Macalester Journal of Physics and Astronomy

Volume 8
Issue 1 *Spring 2020*

Article 11

May 2020

Shape Model of Potentially Hazardous Asteroid 1981 Midas from Radar and Lightcurve Observations

Riley McGlasson
Macalester College, rmcglass@macalester.edu

Shape Model of Potentially Hazardous Asteroid 1981 Midas from Radar and Lightcurve Observations

Abstract

We report observations of potentially hazardous, Apollo-class asteroid 1981 Midas, which passed 0.090 au from Earth (35 lunar distances) on March 21, 2018. During this close approach, Midas was observed by radar both from the Arecibo Observatory on March 21 through 25 (five nights), and from NASA's Goldstone Deep Space Communications Complex on March 19 and 21. These radar observations yielded one-dimensional continuous-wave spectra and two-dimensional delay-Doppler images. In addition, there have been optical lightcurve observations of Midas during four apparitions (1987, 1992, 2004, and 2018), which showed a rotation period of 5.22 hours. Midas has an absolute magnitude of H = 15.2. By combining the lightcurves and radar data, we have constructed a shape model for Midas. This model shows that Midas has two lobes separated by a neck which, at its thinnest point, is about 60% of the width of the lobes. From our model, we also confirm the lightcurve-derived rotation period and show that Midas has dimensions of 3.33 x 1.99 x 1.85 km +/- 10% and a pole position within 6 degrees of (37^0,-61^0) in ecliptic longitude and latitude.

MACALESTER COLLEGE

Shape Model of Potentially Hazardous Asteroid 1981 Midas from Radar and Lightcurve Observations

by

Riley A. McGlasson

in the

Department of Physics and Astronomy

Advisor: Professor John Cannon

March 2020

MACALESTER COLLEGE

Abstract

Department of Physics and Astronomy

by Riley A. McGlasson

We report observations of potentially hazardous, Apollo-class asteroid 1981 Midas, which passed 0.090 au from Earth (35 lunar distances) on March 21, 2018. During this close approach, Midas was observed by radar both from the Arecibo Observatory on March 21 through 25 (five nights), and from NASA's Goldstone Deep Space Communications Complex on March 19 and 21. These radar observations yielded one-dimensional continuous-wave spectra and two-dimensional delay-Doppler images. In addition, there have been optical lightcurve observations of Midas during four apparitions (1987, 1992, 2004, and 2018), which showed a rotation period of 5.22 hours (Mottola et al. 1995; Wisniewski et al. 1997; Muinonen et al. 2007; Franco et al. 2018). Midas has an absolute magnitude of H = 15.2. By combining the lightcurves and radar data, we have constructed a shape model for Midas. This model shows that Midas has two lobes separated by a neck which, at its thinnest point, is about 60% of the width of the lobes. From our model, we also confirm the lightcurve-derived rotation period and show that Midas has dimensions of $3.33 \times 1.99 \times 1.85$ km $\pm 10\%$ and a pole position within 6° of $(37^\circ, -61^\circ)$ in ecliptic longitude and latitude.

Acknowledgements

I would like to thank Dr. Sean Marshall for his guidance in all things shape modeling, and for helping me continue this research from the summer of 2018 through the completion of this paper. Thanks also to the rest of the Arecibo planetary radar group, Drs. Flaviane Venditti and Anne Virkki, for teaching me all about planetary radar during my time at Arecibo.

I would also like to give special thanks to Dr. John Cannon, my advisor throughout these 4 years at Macalester. He introduced me to this wonderful world of astronomy, and encouraged me to pursue research opportunities like the one that produced this research.

More thanks go to my committee, Drs. Anna Williams, Sean Marshall, and John Cannon, for their invaluable comments on this document.

A massive thanks goes also to the residents of OLRI 404 over these past four years, you have pushed and inspired me and I cannot wait to see where you all end up.

Thank you also to Lance A. M. Benner, Marina Brozović, Shantanu P. Naidu, Jon D. Giorgini, Betzaida Aponte, Alan W. Harris, James W. Young, Guy Wells, Daniel Bamberger, Jeff Tobak, and Marek Husarik for the use of their unpublished Midas observations.

This research was supported by the Arecibo Observatory Research Experience for Undergraduates program, National Science Foundation grant 1559849. This research also was supported by NASA's Near-Earth Object Observations Program through grants NNX13AQ46G and 80NSSC18K1098. The Arecibo Observatory is a facility of the NSF, operated under cooperative agreement by the University of Central Florida in alliance with Yang Enterprises Inc. and Universidad Ana G. Mendez.

Contents

List of Figures

List of Tables

CHAPTER 1: Introduction

1.1 An Overview of this Thesis

In this thesis, I will describe the shape modeling process and resulting three-dimensional shape model of the potentially hazardous asteroid 1981 Midas.

In Chapter 2, I provide a review of the existing body of knowledge regarding the near-Earth asteroid population.

Chapter 3 addresses methods used in radar astronomy, both continuous wave Doppler spectra and delay-Doppler images. This chapter also discusses the capabilities of the two telescopes used for radar observations: the Arecibo 305 meter telescope in Puerto Rico and the Goldstone Solar System Radar at the Goldstone Deep Space Communications Complex in California.

Chapters 4-6 discuss the subject of this work, asteroid 1981 Midas. I present the radar and lightcurve observations of Midas in Chapter 4. I then discuss the software and process used for developing the shape model in Chapter 5 and finally the resulting model in Chapter 6.

1.2 Motivation

Near-Earth asteroids are exciting laboratories for planetary science. From them, we can learn about the conditions present in the early Solar System as well as study potential collision hazards and mitigation strategies. Developing shape models for asteroids of interest is a crucial step in achieving these science goals because it allows for the planning of spacecraft missions to visit these asteroids for in situ measurements and sample collection. Additionally, deflection methods for potential collision hazards require detailed knowledge of the asteroid's properties.

Asteroids formed in the early Solar System at the same time as the planets were forming. These small bodies formed from leftover material that was not incorporated into the planets. Even though they have been somewhat altered by space weathering processes or collisions, they still contain primitive material from the time of formation. By studying asteroids, we can analyze this primitive material and learn more about the conditions and evolution of our early Solar System.

Our ability to study asteroids in detail has increased greatly throughout the years. Detailed radar observations and enhanced modeling software have improved our ability to accurately develop asteroid shape models, allowing for higher quality analysis of asteroid properties and dynamics. The accuracy of asteroid shape models was most recently tested in the OSIRIS-REx sample return mission to asteroid Bennu, a potentially hazardous carbonaceous asteroid (Lauretta et al. 2017). The choice of Bennu as the mission target was largely influenced by the existence of a shape model from ground-based radar and lightcurve observations that was published in Nolan et al. (2013). In order to land the spacecraft on the surface to gather samples, a detailed shape model like this one was required. After arriving at Bennu, another shape model was produced from OSIRIS-REx images and the dimensions were found to be within 2% of the dimensions predicted by the ground-based shape model created from radar observations (Nolan et al. 2019).

CHAPTER 2: The Near-Earth Asteroid Population

2.1 Spectral Classification

The development of a spectral taxonomy has been an ongoing project in the area of asteroid science, and applies to the whole asteroid population, not just the near-Earth population. The first modern taxonomy was developed by Chapman et al. (1975) where they combined spectrophotometry, polarimetry, and radiometry to divide asteroids into three groups: carbonaceous (C), silicaceous (S), or unusual (U). This taxonomy was refined and new classes were added based on the high volume of new asteroid research.

Nine years later, Tholen (1984) identified various inadequacies in the old taxonomy and proposed a new one. This new taxonomy would divide the asteroid population into 14 classes based on eight-color spectra and albedo measurements. Based on a larger sample of asteroids than earlier taxonomies (405 with high-quality data), the Tholen taxonomy was able to eliminate the catch-all "unusual" class that grouped together asteroids with significantly different spectral characteristics and split it into more distinct classes (Tholen 1984). In agreement with the Chapman et al. (1975) taxonomy, the most heavily populated classes in the Tholen taxonomy are the carbonaceous (C) and silicaceous (S) classes.

The Tholen taxonomy became the standard asteroid taxonomy and held that distinction for many years. Even today it is used, but the Small Main-belt Asteroid Spectroscopic Survey II (SMASSII) classification system developed by Bus & Binzel (2002b) has become the new standard. The SMASSII taxonomy was developed using visible-wavelength spectra from the Small Main-belt Asteroid Spectroscopic Survey (SMASS) and builds on the previous work done by Tholen (1984). The two taxonomies are similar, however unlike the Tholen taxonomy, SMASSII

does not take into account albedo in its classification and is solely based on spectral features. The SMASSII taxonomy was later expanded by DeMeo et al. (2009) to include near-IR observations.

2.1.1 The SMASSII Taxonomy

The SMASSII taxonomy was born out of the second phase of SMASS, which gathered visible-wavelength spectra for 1447 asteroids (Bus & Binzel 2002b). This was a much larger sample size than what any of the previous asteroid taxonomies were based off of, and as such SMASS was able to develop a more robust classification system that built off of the previous work done by Tholen (1984). With the increased use of CCD observations in asteroid spectroscopy, the spectral interval of the SMASS data set did not align with the spectral interval covered by the Eight-Color Asteroid Survey (ECAS) that was used to create the Tholen taxonomy. Additionally, the higher resolution spectra taken by CCDs were able to resolve smaller spectral features than ECAS measurements could. This necessitated the creation of the new taxonomy, which increased the number of spectral classes from 14 to 26, with 12 retaining similar designations to classes from the Tholen taxonomy (Bus & Binzel 2002b). Additionally, a statistically robust sample like this was able to produce a better picture of the heliocentric distribution of spectral types throughout the main-belt and near-Earth asteroid populations.

The SMASSII taxonomy retained the three main spectral complexes S (siliceous), C (carbonaceous), and X (other) that were present in the previous taxonomies. As can be seen in Figure 2.1, these three historic groupings represent a strong bimodal distribution between the S and C complexes (Bus & Binzel 2002a). While the X complex does not have as distinct of a grouping without factoring in albedo measurements, including this class in the SMASSII taxonomy would not only help preserve the structure of previous taxonomies, but also leave room for further study of the relationship between albedo and spectra within this group of asteroids. Because there was a large overlap between the asteroids observed by SMASS and those included in previous taxonomies, Bus & Binzel (2002b) were able to preserve this X complex even though SMASSII did not include albedo measurements. In addition to the three main spectral complexes, Figure 2.1 shows

some points located outside of the boundaries of these groups. SMASSII was large enough to be able to more closely analyze these outliers and develop spectral classes to encompass them.

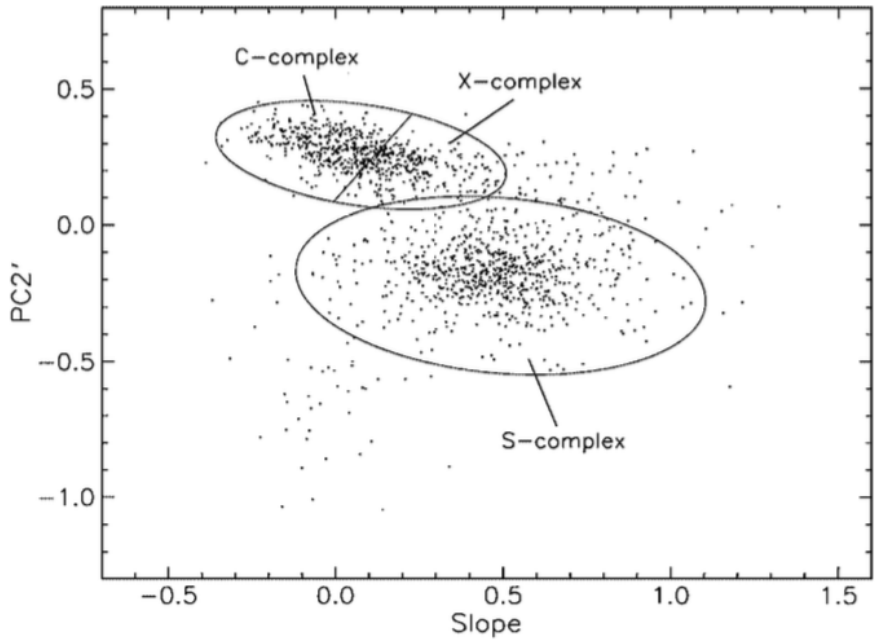

FIGURE 2.1: From Bus & Binzel (2002b), plot of SMASSII asteroids as the PC2' spectral component vs. spectral slope (slope of line fit to each spectrum, proportional to reflectance/wavelength) with the S, C, and X complexes marked. In the SMASSII data reduction, the PC2' component is sensitive to the strength of the 1-μm silicate absorption band, with more negative values corresponding to deeper 1-μm absorption bands.

In order to divide the heavily populated S-complex into more meaningful classes, Bus & Binzel (2002b) started with the asteroids located around the perimeter of the complex, being sure to preserve the A, Q, and R classes from the Tholen taxonomy. The K class is another class outside of the center of the S-complex that was adopted from previous taxonomies (Tedesco et al. 1989). SMASSII identified 35 asteroids with spectra similar to K type asteroids, but with a steeper UV slope, which led to the creation of the L-class of asteroids. The identification of these outer S-complex classes (A, K, L, Q, and R) is closely tied to the classification of the inner ring of classes within the S complex, Sa, Sk, Sl, Sq, and Sr. Creating the outer classes first allowed for the easy identification of asteroids that are in between the average S-complex asteroids, which were placed in the S class. These "in between" asteroids were placed in the inner classes Sa, Sk, Sl, Sq, and Sr, which indicate

that an Sa asteroid falls somewhere between S and A type asteroids, Sk asteroids fall between S and K asteroids, et cetera. This relationship between classes is visible in Figure 2.2, where the Sq spectra falls in between S and Q spectra, the Sr spectra is between the S and R spectra, and all of these intermediate spectra visually look like they have the average shape of the two classes they lie between.

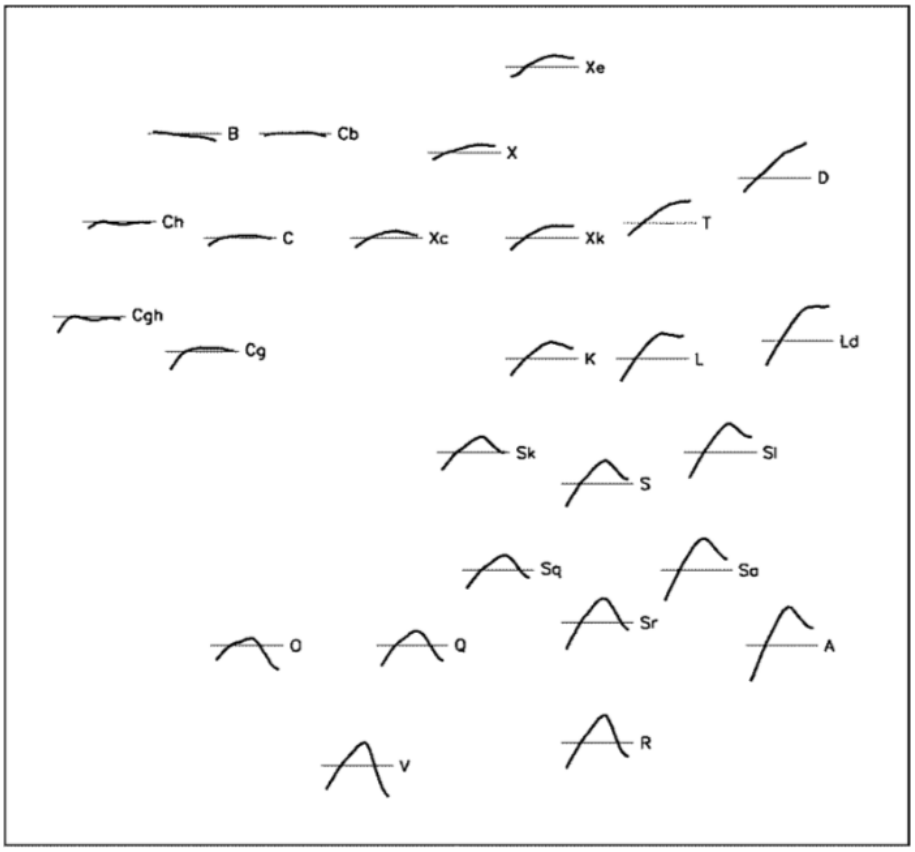

FIGURE 2.2: From Bus & Binzel (2002b), the average spectra for all 26 SMASSII taxonomic classes. Each of these spectra show average reflectance plotted as a function of wavelength from $.44 - .92\mu$m. The spectra are arranged in this figure by the relative position of each class in the PC2' vs. slope spectral component space seen in Fig. 2.1 with the classes in the C and X complexes in the upper half of the figure and the S-complex classes occupying the bottom right portion of the figure.

The C-complex classes were divided based on the presence of a deep UV absorption feature or a broad absorption band around 0.7 μm. Based on the data provided by SMASS, Bus & Binzel (2002b) were not able to remain completely faithful to the class definitions developed by Tholen (1984) regarding the differences between G, C, B, and F classes. Those asteroids which were observed to have a .7 μm

absorption band indicative of the presence of phyllosilicates (Bus & Binzel 2002a) received an "h" appended to their C designations, those with a deep UV absorption feature received a "g", and those spectra that had both of these features warranted a designation of "Cgh". Remaining asteroids in the C-complex that had a mostly flat slope and showed well-defined, but not dominant UV features were assigned a C designation without any other letter appended (Fig. 2.2 shows the average C-class spectrum with this apparent absorption in the UV end of the spectrum). The B class asteroids were distinguished by having a negative spectral slope and a nearly featureless spectrum, as is seen in Figure 2.2. An intermediate group was also created to bridge this gap between the B and C classes, called Cb.

Historically, the X complex has been the catch-all class for asteroids with spectra that could generally be described as featureless. The SMASSII observations, with the new addition of CCD spectroscopy, were able to find a set of subtle spectral features that showed that the X complex could no longer be described as featureless and allowed for the division of classes within the X complex (Bus & Binzel 2002b). The asteroids with spectra outside of the average X-class asteroid spectrum were divided into the Xc, Xk, and Xe classes. In a plot of reflectance as a function of wavelength, the Xc and Xk asteroids exhibit a more curved slope (Fig. 2.2), while the Xe class asteroids are separated due to their unique, although weak, spectral characteristics. Most easily isolated of these Xe-class spectral characteristics is a feature located at 0.49 μm.

SMASS also found many asteroids that lie outside of the three main spectral complexes (Fig. 2.1). These clustered into two groups in spectral parameter space: those with steep UV slopes that flatten out after .75μm and those with a deep 1μm absorption line (indicative of mafic silicates like olivine). The asteroids with steep UV slopes could be split into the T, D, and Ld classes and their spectra can be seen in the upper right portion of Figure 2.2. The V class (basaltic achondrites) and O class (ordinary chondrites) were created from the group of deep silicate absorption outliers and can be seen in the bottom left portion of Figure 2.2.

2.1.2 Bus-DeMeo taxonomy

The SMASSII taxonomy was built using optical CCD spectra, but the new Bus-DeMeo taxonomy made use of newly available near-IR data from the SpeX instrument on the NASA Infrared Telescope Facility (IRTF) to extend that taxonomy across a wider set of wavelengths (DeMeo et al. 2009). This taxonomy is very similar to that of Bus & Binzel (2002b), although they have eliminated three of the SMASSII classes (Sl, Sk, and Ld) and created one new class (Sv). Additionally a "w" notation has been adopted, not as an entire class, but as a note to indicate a steeper spectral slope possibly due to weathering of an asteroid due to collisions and irradiation from the Solar wind (further discussion of space weathering is provided in Section 2.3). The three eliminated classes have been redistributed to other pre-existing classes. The asteroids in the intermediate Ld class, with spectra between those of the L and D classes, have been divided into those L and D classes. The Sk and Sl classes have been merged with the S class, with a subset of Sk asteroids being moved to the Sq class. The Sv class was added to account for those asteroids which exhibit absorption features at the same locations as found in the V class, but these features are shallower and the general slope is closer to that which is common among S-class asteroid spectra. The average spectra of all of the Bus-DeMeo classes are presented in Figure 2.3. As the Bus-DeMeo taxonomy is an extension of the SMASSII taxonomy, it still makes use of the optical CCD spectra gathered in the SMASS survey.

2.2 Orbital Classification

Near-Earth asteroids are defined as any asteroid with a perihelion less than 1.3 au. This population is further classified into 4 groups based on their orbits. These classes are the Amors, Apollos, Atens and Atiras[1]. Each class is defined by their semi-major axis and either their perihelion or aphelion distance. Amor-class asteroids have a semi-major axis length greater than 1 au and perihelion distance of between 1.017 au (Earth's aphelion) and 1.3 au, meaning that their orbit is completely exterior of Earth's orbit and can, in some cases, cross Mars' orbit.

[1] https://cneos.jpl.nasa.gov/about/neo_groups.html

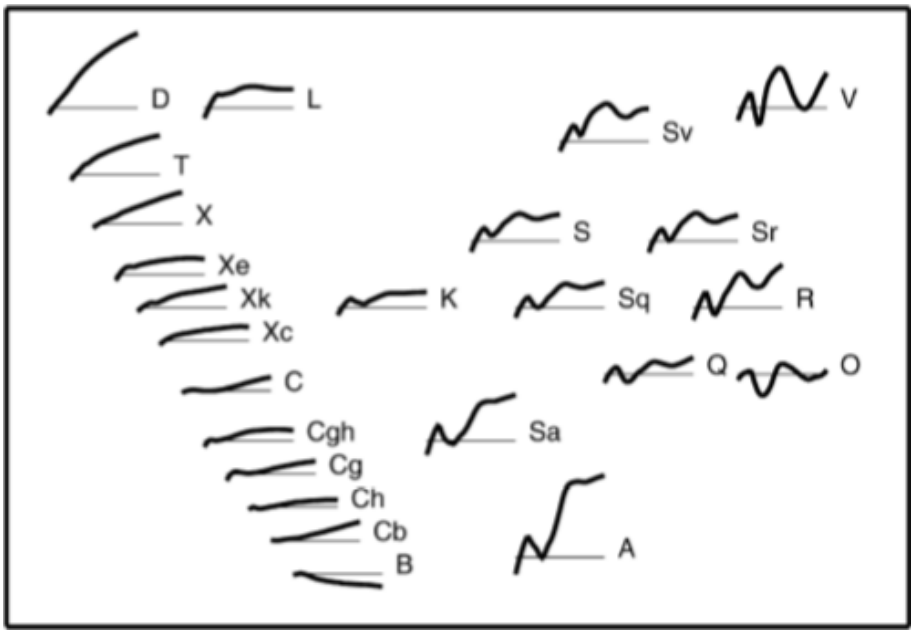

FIGURE 2.3: From DeMeo et al. (2009), the average spectra of the 24 Bus-DeMeo spectral classes. Each of these spectra are plotted with normalized reflectance (vertical axis) as a function of wavelength from $.45 - 2.45\mu$m (horizontal axis). The spectra are arranged in the figure according to the spectral components PC1' vs. PC2'. For the Bus-DeMeo taxonomy, the PC1' component tracks the depth and width of the 1μm absorption line (likely olivine) and the PC2' component tracks the depth and width of the 2μm absorption line (likely pyroxene). This arrangement separates the spectra with subtle features (left portion of the figure) from the spectra with well-defined spectral features.

Apollo and Aten asteroids are all Earth-crossing asteroids, meaning the asteroid will cross Earth's orbit (but not necessarily come close to Earth depending on the orientation of its orbit). However, they differ in that Apollo asteroids have larger orbits – perihelion < 1.017 au and semi-major axis > 1 au. Aten asteroids have a semi-major axis < 1 au and an aphelion $> .983$ au (Earth's perihelion). Atiras have the smallest orbits of all near-Earth asteroids and are harder for us to observe because their orbits are completely interior to Earth's orbit (semi-major axis $<$ 1 au and aphelion $< .983$ au), so observations of these asteroids would be in the direction of the Sun and are therefore much more difficult to obtain.

Greenstreet et al. (2012) present a model that predicts over 90% of NEAs belong to the Amor or Apollo classes. While this number is extreme, it is a sensible prediction based on the assumption that the near-Earth asteroids originate in

the main-belt. Main-belt asteroids are kicked out of orbital resonances by planetary close-encounters with Jupiter and Mars (Greenstreet et al. 2012). Because Jupiter's orbit is on the outside edge of the asteroid belt, encounters with Jupiter tend to either fling asteroids towards the outer solar system or return them to the asteroid belt. In a similar manner, close encounters with Mars on the inside edge of the asteroid belt fling asteroids toward the inner solar system and could account for a significant portion of the current NEA population. By nature of this process, it is more likely that asteroids from the main belt would be flung in to the larger Amor and Apollo-type orbits, and smaller orbits would be increasingly less likely.

2.2.1 Potentially Hazardous Asteroids

As of March 5, 2020, 2066 potentially hazardous asteroids (PHAs) have been discovered[2], but according to the population model from Mainzer et al. (2012) there are expected to be $\sim 4700 \pm 150$ PHAs in total. PHAs are asteroids which come within .05 au of Earth and have an absolute magnitude[3] brighter than 22.0, which corresponds to a diameter of approximately 140 meters (Perna et al. 2016). These asteroids are mostly Apollo or Aten asteroids because their orbits cross that of Earth, but there are some PHAs that are Atiras and Amors with orbits that bring them within .05 au of Earth. PHAs are of special interest because of their potential to collide with Earth and cause damage, but also their large size and close approaches make them an especially easy subset of asteroids to get high-resolution data from.

It is important to gain a thorough understanding of the composition and orbits of these asteroids in order to mitigate potential asteroid collisions. The PHA population has a similarly broad taxonomic distribution to that of the NEA population as a whole (Perna et al. 2016). Perna et al. (2016) find that certain spectral classes of PHAs present a greater threat than others. The carbonaceous (B, C, D, P, T, and Xc) asteroids pose a greater threat than silicaceous S-complex asteroids due to their low-density and porous nature, which our current best methods of asteroid

[2] https://cneos.jpl.nasa.gov/stats/totals.html

[3] For an asteroid, absolute magnitude is the brightness an object would have if measured at 1 au from both the Earth and the sun at zero solar phase angle (Harris & D'Abramo 2015)

deflection (nuclear detonation) are less effective against (Perna et al. 2016). The basaltic (V-type) asteroids are also more threatening because dynamical studies from their parent body, asteroid 4 Vesta, show low minimum orbit intersection distances, which suggests that they are more likely to have closer approaches to Earth (Perna et al. 2016).

The current most promising asteroid deflection methods can be split into three categories: slow push, kinetic impactor, and nuclear detonation (National Research Council 2010). The "slow push" method relies on an external gravity source, usually a spacecraft, to redirect an asteroids orbit. However, the spacecraft would have to be massive to even make a very small change in the asteroid's orbit, so it has very limited feasibility. This method is the most accurately controllable deflection, but it requires decades of advance warning and can only be used with small to medium sized asteroids with diameters of tens to ∼100 meters (National Research Council 2010). Kinetic impactors use high-velocity impacts to divert an asteroid's orbit. This method is within our technological reach, can be implemented with years to decades of advance warning, and could be used for most moderately sized asteroids with diameters ranging from hundreds of meters to ∼1 km (National Research Council 2010). This is an attractive method to have in place, and it will be tested by the Double Asteroid Redirection Test (DART) mission in 2022. Nuclear detonation is the only deflection method currently in place for changing the orbit of large PHAs (diameter greater than 1 km) with little advance warning and will likely remain the backup method in case any of the more desirable methods fail.

Looking away from the dangers of PHAs and towards the scientific benefits, the close proximity and large size of PHAs allow us to gather extremely high resolution data that is otherwise hard to obtain. These PHA data allow us to map asteroids to resolution scales on the order of meters to tens of meters and study orbital parameters with fractional uncertainties of $\sim 10^{-8}$ using ground-based observations (as discussed in Chapter 3). This is necessary in order to study small effects like non-gravitational perturbations. The precise orbital dynamic calculations are also crucial to the success of the above-mentioned asteroid deflection methods.

2.3 Orbital Distribution of Spectral Classes

To draw conclusions about the origins of the near-Earth asteroids, we can compare the spectral energy distribution (spectral features tell us about the composition of an asteroid) of the near-Earth asteroids to that of the main-belt population . Large asteroid surveys like SMASS have made these comparisons possible.

While it is widely accepted that NEAs encompass the full range of spectral classes observed throughout the main belt (Binzel et al. 2002; Sanchez et al. 2013; Binzel et al. 2015; Carry et al. 2016), there are some differences in the distribution of these spectral types. The main-belt asteroid population is dominated by C-complex asteroids (Binzel et al. 2002; Sanchez et al. 2013; Binzel et al. 2015), but this is not the case in the near-Earth asteroid population, which is dominated by S-type asteroids (Fevig 2006; Sanchez et al. 2013; Carry et al. 2016). A comparison of the spectra of C-type vs. S-type asteroids can be seen in Figure 2.3, which shows that C-type asteroids have an almost featureless spectra compared to S-type asteroids. It is important to note that part of this under-representation of C-class asteroids in the NEA population may be due to a selection bias. Because S-type asteroids have higher albedos than C-type asteroids, they are easier to observe (Sanchez et al. 2013). However, even after a strong bias correction is applied, C-type asteroids still are not dominant in the NEA population (Binzel et al. 2002). This trend indicates that there must be a preferential contribution to the NEA population from the inner regions of the main belt because unlike the rest of the main asteroid belt, the inner regions are S-type dominant (Binzel et al. 2002).

Another interesting outlier in the NEA population in comparison with the main-belt population is the higher proportion of Q-class asteroids in the near-Earth population (Binzel et al. 2015) even though they are rarely observed in the main-belt (Bus & Binzel 2002b). This discrepancy is made even more interesting because Q-class asteroids are most spectrally similar to the most common meteorites found on earth (Binzel et al. 2015), leading to the obvious question: where are they coming from?

The most common spectral match between asteroids and the meteorite samples on Earth occurs in the Q-type asteroids (Binzel et al. 2015). However, as can be seen

in Figure 2.3, there seems to be a continuous transition between the spectra of the S and Q classes (Binzel et al. 2004; Fevig 2006; Nakamura et al. 2011; Binzel et al. 2015) where Q-class spectra share similar absorption features with S-class spectra but have a shallower slope. This points to a high likelihood that there are space-weathering processes like resurfacing and irradiation (discussed below) affecting the spectral slope of these asteroids. Space-weathering would increase the slope of unweathered Q-type asteroids, making their observed spectra look like an S-type spectra. This space-weathering hypothesis provides a much sought-after link between observed meteorite composition and near-Earth asteroid spectra, painting a picture of a population of near-Earth asteroids that more closely represents the population of meteorites that have been studied on Earth.

Space-weathering, though it may provide an answer to the meteorite question, also brings up another big question: Why are there more seemingly unweathered (Q-type) asteroids in the near-Earth sample than in the main-belt? If collisions provide the main source of resurfacing, there should be more Q-type asteroids among the main-belt population, where there are more collisions. However, NEAs encounter the gravitational pull of planets more frequently than they collide with other asteroids (Nesvorný et al. 2005). In a statistically significant sample of 100 S and Q type NEAs, Binzel et al. (2010) found that all of the Q-type (unweathered) asteroids in the sample had possibly interacted with Earth in the past 10^5 years, and none of the S-type (weathered) asteroids had any recent Earth encounters. When these Q-type asteroids interact with Earth's gravitational field, the loose regolith on their surface is shaken up because of the large gravitational forces. This shaking is sufficiently large enough to turn over these surface grains and expose fresh unweathered material (Fevig 2006; Binzel et al. 2015). After an encounter like this, the newly resurfaced asteroid would have a Q-type spectrum but will again be subject to slow-acting space weathering mechanisms (irradiation by high energy Solar particles) that will shift the spectrum to an S-type spectrum over time. DeMeo et al. (2014) study this seismic resurfacing effect around Mars and find that Mars, and likely other planets as well, also contributes to this resurfacing of asteroid surface.

The space weathering hypothesis is also supported by the distribution of spectral classes as studied in Fevig (2006), who found that Apollo asteroids, which have

more eccentric orbits and are subject to more collisions and interactions with large bodies, are more dominated by these Q-class asteroids that appear unweathered. Because Apollo asteroids are subject to more gravitational interactions, these apparently unweathered asteroids may have actually been subject to space weathering in the past, but due to a collision or interaction have been freshly resurfaced. Apollo asteroids with less eccentric orbits and Aten asteroids are found to have a mix of Q and S type asteroids, as they both are Earth-crossing asteroids and could possibly interact with Earth's gravity. The Amor class, which is located between Earth and Mars, is less likely to have major collisions or gravitational interactions and is populated by an overabundance of S-type asteroids.

CHAPTER 3: Radar Astronomy

There are only two facilities that actively operate as transmitters for radar operations: the Arecibo 305m telescope in Puerto Rico and NASA's Goldstone Deep Space Communications Complex in California. Other radio telescopes like the Green Bank Telescope can be used as a receiver in conjunction with Arecibo or Goldstone to obtain longer integration times and higher signal-to-noise ratios. These two observatories have complementary capabilities – Arecibo is more sensitive and can detect fainter objects, but Goldstone's steerability allows for coverage of $\sim 80\%$ of the sky (Benner et al. 2015). Goldstone, due to its higher transmitter frequency of 8560MHz (compared to Arecibo's 2380 MHz), is able to produce 3.6x larger bandwidth, so effectively finer Doppler resolution than Arecibo for high signal-to-noise (SNR) objects (Benner et al. 2015). Even though Goldstone has greater sky coverage, Arecibo can detect significantly more near-Earth asteroids due to its increased sensitivity. As a result, only 5% of NEAs bright enough to be observable by Goldstone are too far north or south to be detected from Arecibo (Benner et al. 2015).

Radar observations are the main method of directly imaging NEAs without sending a spacecraft mission to the asteroid (Giorgini et al. 2009). While this is an extremely effective tool to use as a follow-up for optical discoveries, the narrow beam width and $1/r^4$ SNR dependence makes radar an extremely ineffective search method (Giorgini et al. 2009). Accurate astrometry from optical observations is a prerequisite for radar imaging.

Radar observations take the form of continuous wave (CW) Doppler spectra or delay-Doppler images. CW spectra are taken by transmitting a continuous, circularly polarized signal for the round-trip light travel time to the target and then receiving the reflected signal for that same duration. During the receiving portion of the observation, echoes reflected from the asteroid are measured in the opposite (OC) and same (SC) sense polarization as the transmitted signal (Shepard et al. 2004; Virkki et al. 2014).

From the ratio of SC to OC echoes, we can measure the structural complexity of the asteroid's surface at size scales that are approximately equal to the transmitted wavelength (Ostro et al. 2002; Virkki et al. 2014), 12.6 cm at Arecibo and 3.5 cm at Goldstone (Naidu et al. 2016). Reflection of circularly polarized light off of a smooth surface flips the handedness of the light. As a result, after one reflection off of a smooth surface, transmitted right-handed circularly polarized light (RCP) will be received as left-handed polarized light (LCP). Using these properties, we can conclude that if the surface of an asteroid is completely smooth, the circularly polarized signal will be reflected in the opposite polarization, causing the SC/OC ratio to be zero (Ostro et al. 2002). However, if the asteroid's surface is rough at wavelength scales, these properties of reflection will be disrupted and a larger portion of the echo will return in the same polarization state as was transmitted. In addition to characterizing the surface roughness, CW spectra taken at a variety of viewing geometries also are able to constrain the diameter and spin rate by measuring echo power as a function of Doppler shift caused by the rotation of the asteroid. (Taylor et al. 2019a).

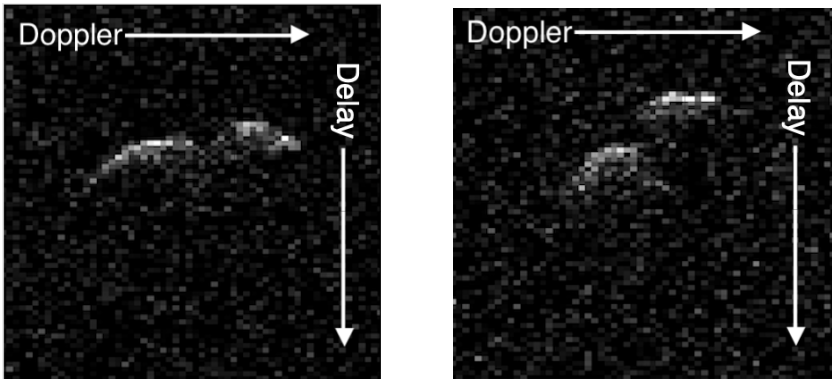

(A) (B)

FIGURE 3.1: Delay-Doppler images of potentially hazardous asteroid 1981 Midas at 2 different points in its rotation. The echo power is plotted with Doppler shifted frequency increasing left to right and delay increasing top to bottom. These images were taken at Arecibo Observatory during Midas's close approach in March 2018. From these images we can see a distinctly bi-lobed object with one lobe about 30% larger than the other.

Unlike CW spectra, delay-Doppler images are created by transmitting a modulated signal where the phase is either flipped or not flipped every baud (the length of time between phase flips). Correlating the returned echos with their modulated

transmitted signal and mapping that signal to the corresponding time delay and Doppler-shifted frequency produces the delay-Doppler image (Taylor et al. 2019a). An example of this type of image is presented in Figure 3.1, which shows two delay-Doppler images of Midas, which appears to be a large bi-lobed asteroid.

The resolution of the delay is dependent on the baud length of the transmitted signal. Choosing the length of the baud (t_{baud}) results in a delay resolution (ΔR) of $\Delta R = c * t_{baud}/2$ (Harcke 2005) where c is the speed of light and the factor of 2 comes from the signal traveling twice the distance to the asteroid (the signal has to travel to and from the asteroid). For example, a baud length of .05 μs results in a delay resolution of $\Delta R = 7.5$ m. The Doppler resolution, as with CW spectra, is dependent on the frequency of the transmitted signal, with higher frequencies resulting in finer Doppler resolution.

Delay-Doppler images are plotted in delay-Doppler phase space, so they do not look like the optical plane-of-sky images that would be taken by a spacecraft, but with sufficient data they can be used to build high-resolution three-dimensional shape models of asteroids. Because radar images are the projection of a three-dimensional object into two dimensions, a many-to-one mapping emerges (any points that have the same delay and Doppler shift are mapped to the same pixel in the radar image) that creates a north-south ambiguity in the images (Ostro et al. 2002; Taylor et al. 2019a). Breaking this ambiguity requires sufficient data from different viewing angles.

Delay-Doppler images are also very useful for unambiguously identifying binary asteroid systems. Binary asteroids comprise only a small subset of the known NEA population, and without delay-Doppler images, it is difficult to distinguish a binary asteroid system from a single elongated asteroid or a contact binary asteroid (Fig. 3.1). As of 2016 there were 54 known binary systems, and 41 of them had been discovered by radar (Brozovic et al. 2016).

Even with delay-Doppler imaging, it can still be difficult to discern any separation between the two lobes. For example, during the discovery of the equal-mass binary asteroid system 2017 YE5 (the most recent discovery of the four known equal mass near-Earth binary pairs), no separation was clear for the first three nights of observations (Taylor et al. 2019b). During following nights, bistatic observations

(radar observations using two telescopes) were coordinated between the Arecibo and Green Bank telescopes. Bistatic observations are occasionally used for especially promising targets where increased frequency resolution is necessary. Using two telescopes with one transmitting and the other receiving the signal eliminates the need to switch between the two modes, and as a result the integration time is only limited by the time the asteroid is able to be viewed by the telescope. Bistatic observations of 2017 YE5 with Arecibo transmitting and Green Bank receiving allowed for sufficient frequency resolution to separate the two lobes of the asteroid in Doppler space and produce the finest resolution images (7.5 m) of any equal mass binary previously observed (Taylor et al. 2019b).

CHAPTER 4: Observations of 1981 Midas

Asteroid 1981 Midas was discovered in 1973 by Charles Kowal at Palomar Observatory (Franco et al. 2018). It is a V-type Apollo-class asteroid that crosses the orbits of Venus, Earth, and Mars, and has been classified as a "Potentially Hazardous Asteroid" (PHA) by the Minor Planet Center[1]. Previous observations have found an orbital semi-major axis $a = 1.777$ au, an eccentricity $e = .650$, and an orbital inclination $i = 39.8°$. Numerous lightcurves of this asteroid have been obtained over the period from 1987-2018, which combined with the recently acquired radar images from its close approach to Earth in 2018 provide a wealth of data at different viewing geometries. This wealth of data combined with Midas's size and close orbit to Earth make Midas a promising and high-priority target for shape modeling.

4.1 Lightcurve Observations

We have obtained optical lightcurve data from 20 nights between the years of 1987 and 2018. A summary of these observations is given in table 4.1. Lightcurves are much easier to obtain than radar data because they can be taken when the asteroid is at farther distances than can be seen with radar, and are often used to obtain the absolute magnitude and place constraints on the size of the asteroid. From these optical observations, Midas has been found to have an absolute magnitude (for a Solar System object, absolute magnitude is defined to be the object's magnitude if observed at a distance of 1 au from both the observer and the Sun, and at zero phase angle) of H = 15.2[2]. Additionally, the large lightcurve amplitudes of these observations suggest that Midas is a highly elongated object (example lightcurves plotted with model lightcurves are shown in Figures A.7, A.8, A.9). The large quantity of lightcurves available enabled us to better determine the position of Midas's rotational axis (hereafter called pole position), and were especially crucial in determining a preference between a northern and southern pole model.

[1] JPL Small-Body Database: https://ssd.jpl.nasa.gov/sbdb.cgi?sstr=2001981
[2] https://ssd.jpl.nasa.gov/sbdb.cgi?orb=1;sstr=1981

Given the north-south ambiguity present in radar images (discussed in Section 3), lightcurves are necessary for breaking this ambiguity and determining a preference between models.

We were not originally aware of the four nights of lightcurve observations from March 5-11, 2018 (listed in Table 4.1) taken by Husarik at the Skalnaté Pleso Observatory (Slovakia), so they were not originally used in the shape model. Once we obtained them, later on in the modeling process, they were incorporated and acted as an independent check on the progress of our shape model. They covered a range of phase angles that we previously did not have coverage for (see Table 4.1), and as such they provided more evidence for a preferential southern pole model over a northern model (for further discussion, see Section 5.3).

4.2 Radar Observations

During the March 2018 close approach of Midas (0.0896 au or 34.9 lunar distances), radar data was acquired over 2 nights by the Goldstone Solar System Radar and 5 nights by the Arecibo 305m telescope. Unfortunately, at the time these data were taken, neither Goldstone nor Arecibo were capable of transmitting at full power. These observations are summarized in Table 4.2. A more detailed discussion of radar astronomy can be found in Chapter 3.

Over 6 of these nights, we obtained continuous wave (CW) spectra during which a continuous, circularly polarized signal is transmitted, and the reflected power is measured as a function of frequency. Both opposite sense (OC) and same sense (SC) polarization echos were measured. For these observations, the SC measurements had lower signal to noise ratios (SNR) than the OC measurements, but we found the SC data to still have high enough SNR to be used in our model. This is an indicator of a surface that is rough at wavelength scales (refer to Chapter 3 for further discussion).

Delay-Doppler observations were obtained on 5 of these nights. For delay-Doppler observations the transmitted signal is pseudo-randomly modulated in order to resolve the reflected signal in both Doppler frequency and delay. These images

were taken with baud lengths of .2 μs and .5 μs, which correspond to effective delay resolutions of 30 m and 75 m, respectively. Even without the model, we can directly infer from these high resolution images (for example, those in Fig. 3.1) that Midas appears to be a bilobed object with one lobe approximately 30% larger than the other.

Table 4.1: Lightcurve Observations

Observing Date (UT)	t· (HH:MM)	Δt (h)	RA (hours)	DEC (°))	Δ (au)	α(°)	Observer
25 September 1987	02:51	4.6	20.4	-18.4	0.094	52	Harris, Young
26 September 1987	02:45	4.2	20.6	-11.9	0.105	49	Harris, Young
27 September 1987	02:35	1.1	20.7	-06.7	0.119	47	Harris, Young
28 September 1987	02:39	1.5	20.8	-02.6	0.133	46	Harris, Young
29 September 1987	02:28	5.0	20.9	00.9	0.148	45	Wisniewski
6 March 1992	06:57	2.5	16.4	-09.4	0.165	71	Mottola
7 March 1992	06:35	2.8	16.6	-13.3	0.155	74	Mottola
8 March 1992	06:09	3.3	16.9	-17.7	0.147	78	Mottola
9 March 1992	08:06	1.4	17.3	-22.9	0.140	83	Mottola
10 March 1992	06:17	3.1	17.6	-27.5	0.136	87	Mottola
15 September 2004	02:51	2.6	04.6	+60.4	1.994	26	Torppa
5 March 2018	21:19	3.2	12.9	+45.3	0.263	37	Husarik
8 March 2018	21:27	6.1	12.6	+47.3	0.219	38	Husarik
9 March 2018	20:39	7.2	12.4	+47.9	0.205	38	Husarik
11 March 2018	20:37	6.8	12.0	+49.5	0.178	40	Husarik
13 March 2018	21:03	0.3	11.4	+50.8	0.152	42	Wells, Bamberger
16 March 2018	20:39	0.3	10.0	+50.8	0.118	49	Wells, Bamberger
19 March 2018	21:12	0.5	08.0	+43.2	0.094	63	Wells, Bamberger
21 March 2018	18:36	4.3	06.8	+32.4	0.089	76	Baj
22 March 2018	18:29	3.9	06.3	+25.6	0.091	83	Baj

This table lists the observing date and starting time (t·) in UT, duration of the observation (Δt) in hours, RA and DEC of the asteroid at the start of the observation rounded to the nearest tenth of an hour, distance (Δ) of the asteroid at the start of the observation in au, the phase angle of the asteroid (α) in degrees, and the observer.

TABLE 4.2: Radar Observations

Observing Date (UT)	Type	Telescope	Runs	Baud(μs)	spb	Power (kW)	Receive Time (UT HH:MM:SS-HH:MM:SS)	RA (hours)	DEC (°))	Δ (au)
2018 March 19	CW	G	36	-	-	100	02:46:44-04:43:50	08.5	+46.3	0.099
	CW	G	9	-	-	100	06:15:41-06:40:08	08.4	+45.8	0.098
2018 March 21	CW	G	33	-	-	100	01:06:39-02:45:09	07.2	+36.9	0.090
	CW	G	19	-	-	100	03:52:42-04:48:48	07.2	+36.3	0.090
	CW	G	27	-	-	100	05:32:07-06:51:36	07.1	+35.9	0.090
	CW	A	3	-	-	370	22:17:55-22:25:17	06.7	+31.3	0.090
	Delay-Doppler	A	9	.5	1	376	22:32:01-22:59:18	06.7	+31.3	0.090
	Delay-Doppler	A	20	.2	4	359	23:18:41-00:17:04	06.7	+31.1	0.090
2018 March 22	CW	A	7	-	-	339	21:22:09-21:41:44	06.2	+24.7	0.091
	CW	A	1	-	-	347	21:48:01-21:49:24	06.2	+24.6	0.091
	Delay-Doppler	A	10	.2	4	341	22:00:26-22:29:08	06.2	+24.6	0.091
	Delay-Doppler	A	26	.5	1	358	22:37:26-23:54:39	06.2	+24.4	0.091
2018 March 23	CW	A	8	-	-	377	20:53:21-21:18:51	05.8	+18.0	0.094
	Delay-Doppler	A	13	.5	1	395	21:26:06-22:06:18	05.8	+17.9	0.095
	Delay-Doppler	A	13	.5	1	391	22:26:03-23:06:51	05.8	+17.6	0.095
	Delay-Doppler	A	4	.5	1	389	23:18:57-23:29:54	05.7	+17.4	0.095
2018 March 24	CW	A	8	-	-	388	20:28:52-20:53:59	05.4	+11.8	0.100
	Delay-Doppler	A	33	.5	1	395	20:59:34-22:55:58	05.4	+11.7	0.100
2018 March 25	CW	A	8	-	-	390	20:19:56-20:48:05	05.1	+06.2	0.108
	Delay-Doppler	A	20	.5	1	394	20:57:03-22:20:18	05.1	+06.0	0.108

This table lists the observing date in UT, the type of radar data, the telescope which acquired the data (G for Goldstone, A for Arecibo), the number of runs conducted, the baud length used (if delay-Doppler), the samples per baud (spb, for delay-Doppler), the power of the transmitted signal, the receive start-end time, the RA and DEC at the beginning of the observation rounded to the nearest tenth of an hour, and the geocentric distance of the asteroid at the beginning of the observation.

CHAPTER 5: SHAPE Modeling

5.1 SHAPE Software

To develop this model of Midas, we used the SHAPE software created by Hudson (1994) and later enhanced significantly by Magri et al. (2007). SHAPE is a modeling software that combines radar data, lightcurves, and asteroid ephemeris data to find a best-fit model by iterating through a set of parameters. These parameters include optical and radar scattering properties, spin state parameters, lengths of each of the 3 axes, and the positions of the vertices themselves. For any fit, these parameters can be held constant at a user-specified value or allowed to vary. For the parameters that are allowed to vary, SHAPE varies each parameter slightly to minimize the chi-squared value of the model. SHAPE calculates chi-squared by computing a model frame and comparing that to the corresponding data for each frame of delay-Doppler, lightcurve, and CW observations. We also apply penalty functions to mathematically discourage unphysical models (thin rod-like models, spiky 'sea urchin' models). These unphysical models are discussed more in section 5.3.

Developing a shape model is a many dimensional problem, and is not a trivial problem to solve even with the SHAPE modeling software. SHAPE often gets stuck in local minima of this many dimensional space, so human judgement is necessary to guide SHAPE to the best-fit model. Getting SHAPE out of these local minima can require adjusting penalty weights or manually adjusting the position of vertices using Blender, an open-source 3D computer graphics software[1] that was first used in asteroid shape modeling by Crowell et al. (2017). We use this software to access the individual vertices of the 3D model and shift their positions by dragging the points by hand. It is important to note that Blender does not use actual data, so it is used as a supplemental tool to shift individual vertices when SHAPE gets stuck rather than a data-driven modeling tool.

[1] https://www.blender.org/

5.2 Modeling Process

Typically, an asteroid shape model starts with a simple ellipsoid or ovoid model that the data are applied to. For Midas, we started with an ovoid model to get rough dimensions of the asteroid, but then, because radar images indicated that Midas is a bilobed object, we applied those base dimensions to a preexisting asteroid model of another bilobed asteroid, 1996 HW1 (Magri et al. 2011). We chose to use another bilobed asteroid as a starting model because with a software like SHAPE that makes small, iterative adjustments, it is much easier and quicker to shift a preexisting "neck" between the lobes of the asteroid than it is to create a neck in a simple ovoid model. This progression from simple ovoid to 1996 HW1 to Midas models is shown in Figure 5.1.

The two main things we look to find in a shape model are the position of the rotation axis (pole position) and the actual shape of the asteroid. When constructing the shape model of Midas, we alternated refining the pole position and adjusting the positions of the vertices. SHAPE is not very good at determining an accurate pole position because changing the pole position requires compensating with changes in other parameters as well. Because this version of SHAPE only changes one parameter at a time, changing only the pole longitude or latitude almost always results in a worse chi-squared value. To find an accurate pole position, we manually searched a broad spacing of pole positions and gradually performed finer searches around our best-fit pole positions. A plot of example grid search results is shown in Figure 5.2. Given the variety of viewing geometries in our lightcurve observations, these data proved to be the most useful in determining the pole position. To adjust the positions of the vertices, we would take the best model from the most recent pole position search, hold the pole position constant, and allow the position of each vertex to vary.

SHAPE would often get stuck in a local chi-squared minimum, so we had to manually make larger changes to the model. Blender became an invaluable tool to do this, as it allows for adjustment of the positions of individual vertices as well as the addition of vertices in places that need higher resolution. For Midas, we had some difficulties fitting the vertices in the neck area, so we added more

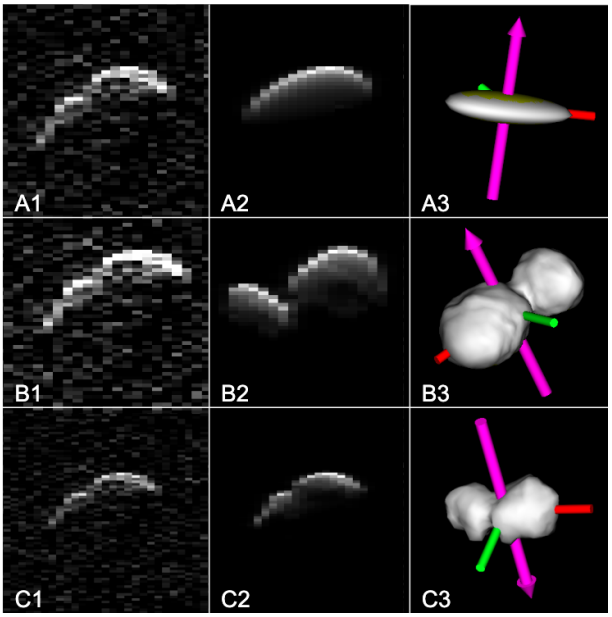

FIGURE 5.1: Progression of three different model types: ovoid, 1996 HW1, and Midas. Row A shows the comparison of a delay-Doppler frame of Midas (A1), delay-Doppler ovoid model frame (A2), and simulated plane-of sky image (A3) of the same view as the delay-Doppler frames. In the plane-of-sky view, the pink arrow shows the rotational axis and the red and green lines show the long and intermediate axes, respectively (the short axis is aligned with the rotational axis). Row B shows the same comparison, but using the 1996 HW1 model from (Magri et al. 2011) instead of the ovoid model. Row C shows that comparison but with a later stage model of Midas. The 1996 HW1 model is a bad fit for the data, but it has 2 lobes (B2) that appear to be of the same proportions as the 2 lobes visible in the data (B1). This is a much easier starting point for SHAPE to fit to the data than an ovoid model (A2) is.

vertices there to give SHAPE the ability to more finely adjust the neck geometry. SHAPE would often get stuck while making adjustments in this area, so we used Blender to make large enough vertex shifts for SHAPE to be able to get away from the local chi-squared minimum it was stuck in. Then, by putting the model edited in Blender back into SHAPE and running a model where we let all of the vertices vary, SHAPE would generally produce a model much closer to the data than before the edits were made in Blender. Of course, this is highly dependent on the ability to make reasonable adjustments by eye, as radar data can be difficult to interpret.

The north-south ambiguity present in radar imaging (discussed in section 3) creates a challenge for shape modeling. In many cases, it is only possible to determine

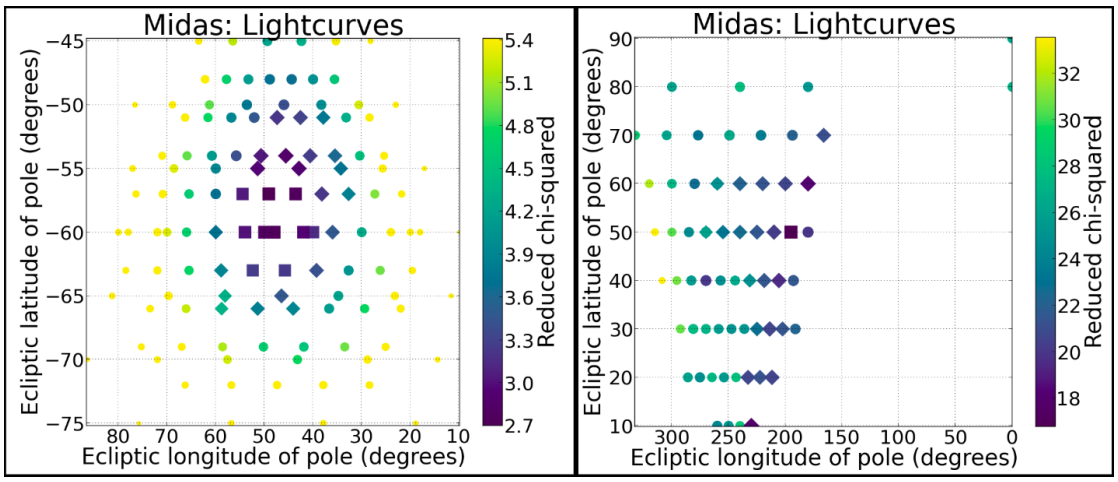

FIGURE 5.2: A grid search (left, southern; right, northern) to determine the pole position of the model using lightcurve data. Ecliptic longitude and latitude are plotted on the x and y axes, respectively. Each point is color coded with the reduced chi-square value of the model, with purple indicating a low reduced chi-square value and yellow indicating a higher reduced chi-squared value. Looking at these figures, it becomes clear that the northern models are much worse fits for the lightcurve data.

a preferential north pole and south pole model, rather than a preferential overall model. We began constructing our model with this in mind, running fits on both a northern model and southern model separately. By doing this, we remove the bias towards either orientation that would arise from running a southern pole position search on a vertex model that had been created with a fixed northern pole position (which would create a bias against the southern pole position) or vice versa.

Eventually, we were able to rule out our northern model (where the rotation pole direction is north of the ecliptic plane). This was largely due to having lightcurves that were taken when Midas was at a variety of viewing geometries (the variety of phase angles observed is shown in Table 4.1). Being one of the earliest discovered near-Earth asteroids, there are lightcurve observations available from as early as 1987. By applying these lightcurve data, we were able to see that the northern pole models not only have higher chi-squared values, but also are visibly worse fits (see Fig. 5.4).

5.3 Bad Models

Some models produced egregiously bad fits, emphasizing the need for penalty functions. Penalty terms get added to the chi-squared to discourage SHAPE from accepting physically unrealistic models. Without the implementation of penalty functions, SHAPE begins to treat unphysical noisy pixels as real data. This produces models that have egregious spikes ("sea urchin models"), but can be mitigated by applying a nonsmooth penalty that mathematically discourages adjacent faces that are not close to being coplanar. We also sometimes get flat "pancake models" models (Fig. 5.3A), that we fix by applying a flattening penalty that discourages models where the dimensions of the two shortest axes are very different. Enforcing too heavy of penalties, however, can also produce unphysical models. For example, too heavy of a flattening penalty results in rod-like "pencil" models (Fig. 5.3B).

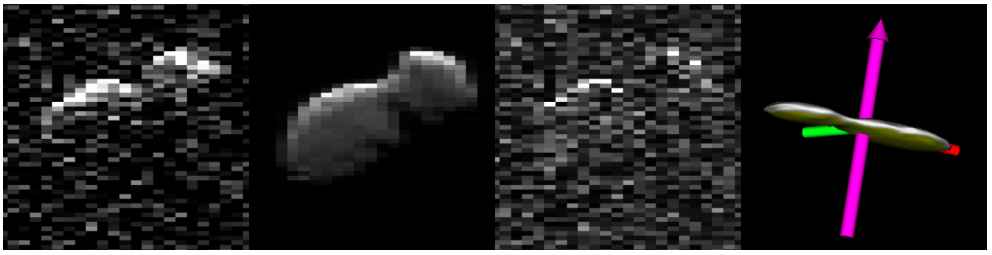

(A)

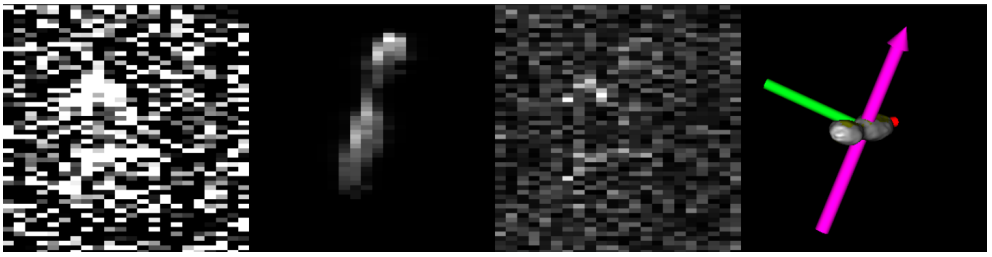

(B)

FIGURE 5.3: Examples of two types of bad models: "pancake" models (A) and "pencil" models (B) where the frames show, from left to right, delay-Doppler data, model, residuals, plane-of-sky view of the model. In the plane-of-sky view, the pink arrow shows the rotational axis and the red and green lines show the long and intermediate axes, respectively (the short axis is aligned with the rotational axis). Pancake models are unphysical, but can be fixed with the application of a flattening penalty function. Pencil models are the result of two heavy of a flattening function.

Our other type of bad model was our northern pole model. This started out as a viable model, but after folding in additional lightcurve data it was clear that a northern pole model did not fit the data. These models could fit the delay-Doppler images or the lightcurves, but not both. In the example shown in Figure 5.4, the model is good fit for the lightcurve data and a terrible fit for the delay-Doppler images, while the example in Figure 5.5 is a bad fit for the lightcurve data and an okay fit for the delay-Doppler images.

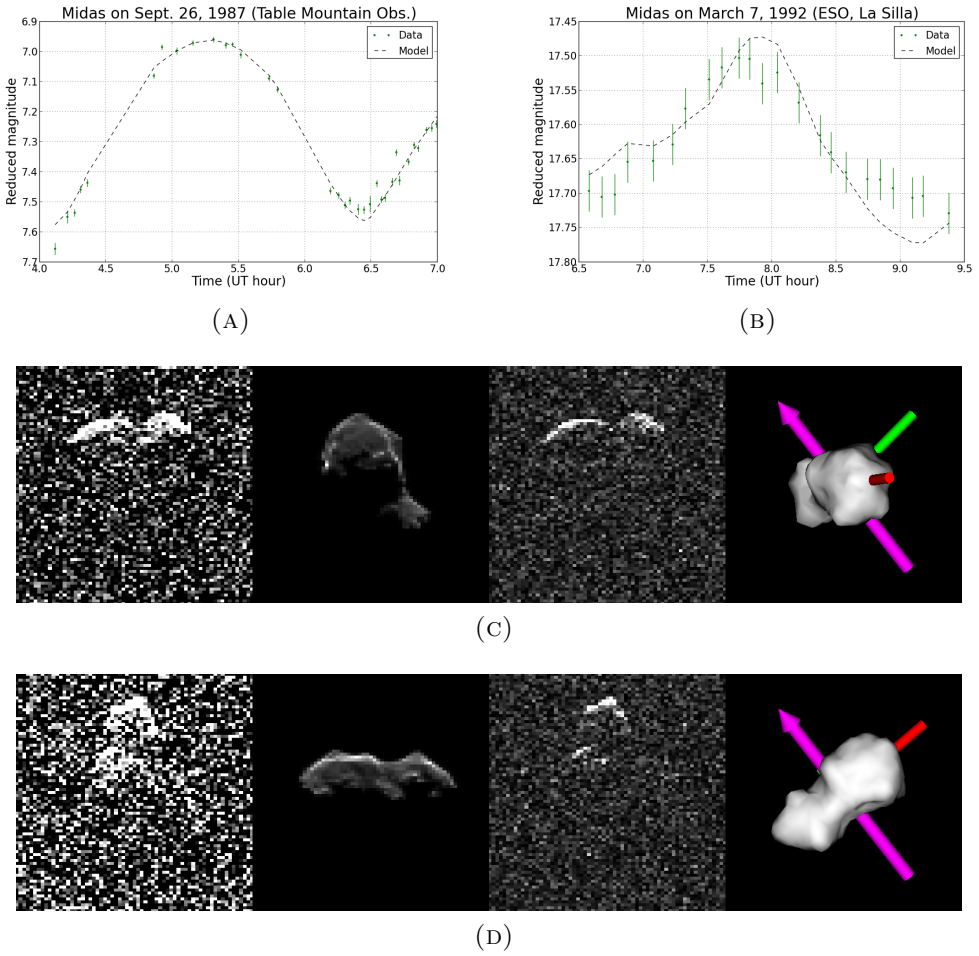

(A) (B)

(C)

(D)

FIGURE 5.4: Example views of the best northern model for the lightcurve data. The delay-Doppler frames are organized as in Fig. 5.3. The model is a good fit for the lightcurve data (A, B), but is a terrible fit for the delay-Doppler images (C, D). This is compelling evidence to confirm the preference of a southern model over this northern model.

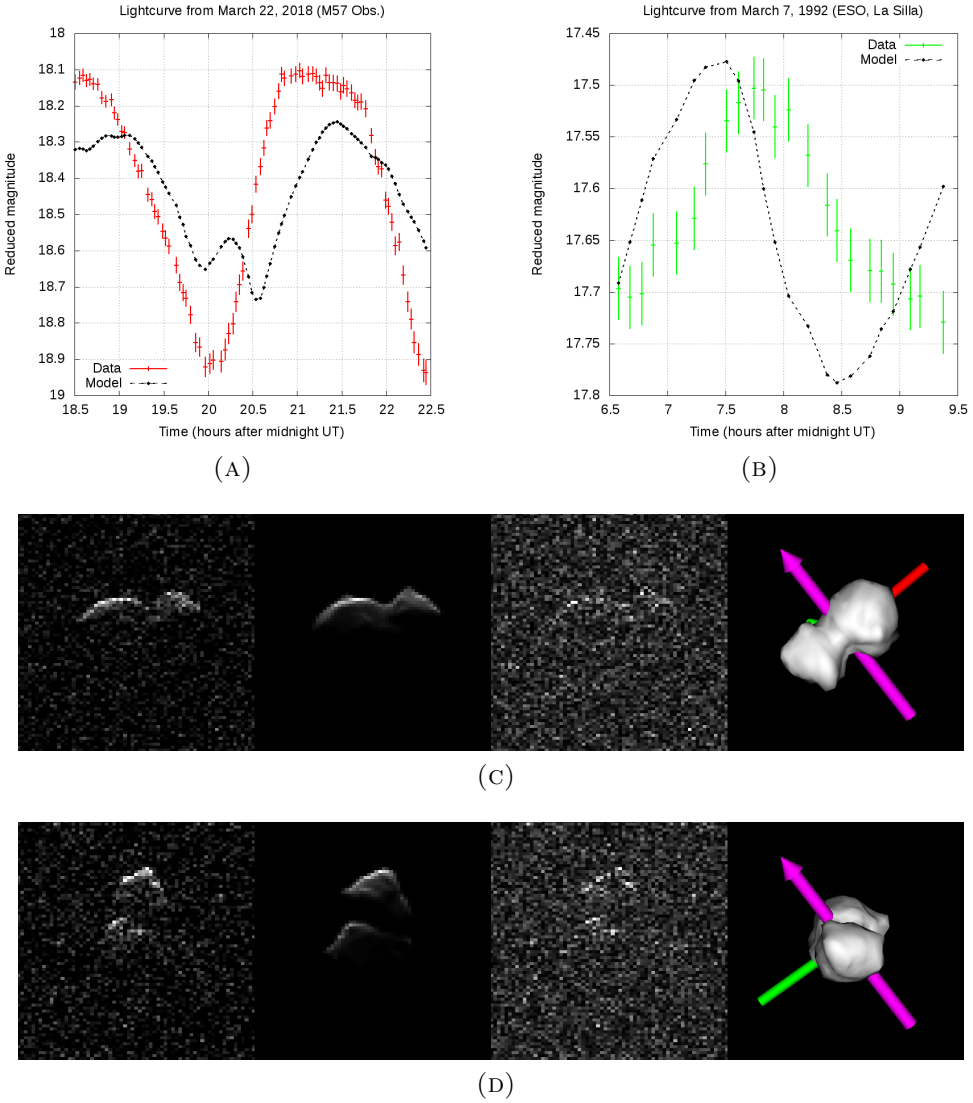

FIGURE 5.5: Example views of the best northern model for the radar data. The delay-Doppler frames are organized as in Fig. 5.3. The model is a bad fit for the lightcurve data (A, B), but is an okay fit for the delay-Doppler images (C, D). This is further evidence to confirm the preference of a southern model over this northern model.

CHAPTER 6: Results and Conclusions

6.1 Pole Position

Finding the direction of the rotational axis (pole position) in terms of ecliptic longitude and latitude was one of the more human-power intensive parts of the shape modeling process because SHAPE is not very good at determining the correct pole position. Because of this, we manually searched a broad spacing of fixed pole-positions (10° separation over a region of ±45° from the previous best-fit pole position). From those results, we tested finer angular separation (5°, then 3°, then 1°) over smaller regions around our best pole positions to find a final pole position that is within 6° of (37°,−61°).

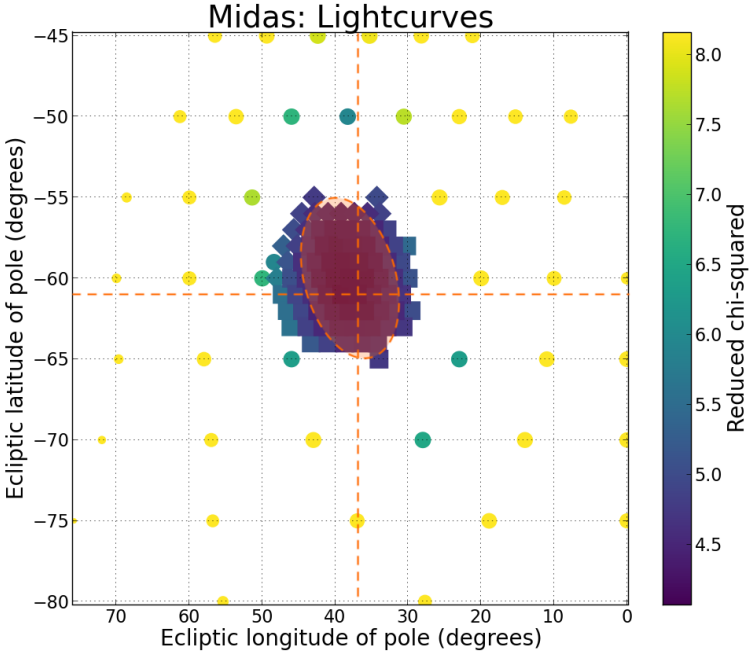

FIGURE 6.1: Plot of pole position chi-squared values. Longitude is plotted on the horizontal axis, latitude on the vertical axis, and it is colored by reduced chi-squared value of the lightcurve data. We show the latitude and longitude error bars as orange regions, with the overlapping region being the overall 1σ region for the pole position, with our best model shown by the dashed orange line.

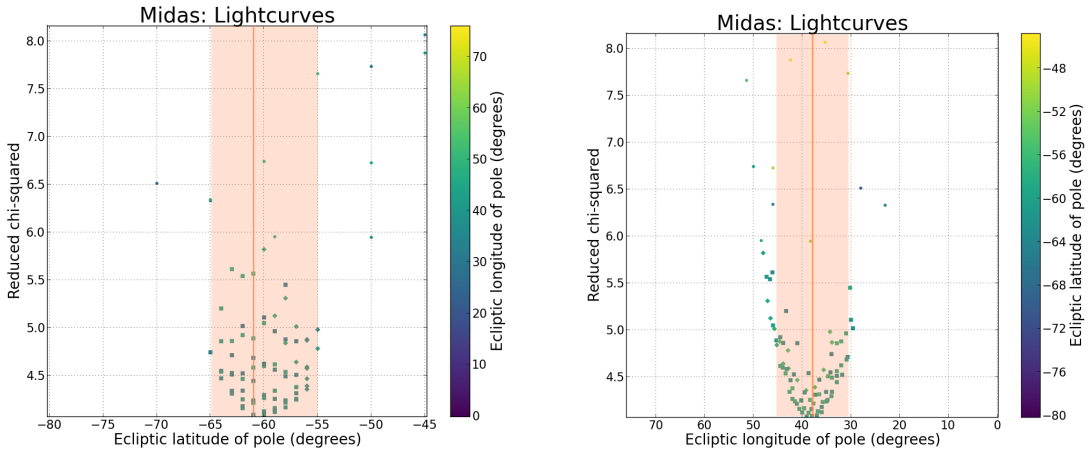

(A) (B)

FIGURE 6.2: Uncertainty analysis for pole position. Each data point represents an individual SHAPE model of Midas. For plot A, data points are plotted with latitude of the pole on the horizontal axis, reduced chi-squared value of the lightcurve data on the vertical axis, and colored according to longitude. Plot B is the same as A, but with color bar and horizontal axis switched. We take 1σ to be the furthest distance in degrees before the reduced chi-squared increases by 1. This bound is shown by the orange shaded region, with the smallest reduced chi-squared model indicated by a solid orange line, and (if different) the location of the best model indicated by a dashed orange line.

In order to determine the uncertainty of this pole position, we ran a series of models with fixed pole positions across a grid with 5° spacing centered around (37°,−61°) covering 20° in every direction. We then ran a finer search with 1° covering ±5° around (37°,−61°). For these models, we allowed SHAPE to change the scale of each axis and the rotation phase. For all pole position error analysis, we use only the reduced chi-squared of the lightcurve data because they proved to better constrain the pole position than the radar data. A plot of the location of these models and the resulting reduced lightcurve chi-squared values is given in Figure 6.1. It should be noted that a good model should have a reduced chi-squared close to 1.0, but even our best models have reduced lightcurve chi-squared values closer to 3.0. We believe that this is due to underestimation of error bars in some of the lightcurve observations, where it can be seen that the typical vertical scatter between neighboring points is larger than the error bars (for example, A.7), which is unreasonable. To determine a 1σ bound on this pole position, we made plots of the latitude and longitude versus reduced chi-squared (Fig. 6.2). By inspection, we determine 1σ to be the distance from the best model to where the reduced

lightcurve chi-squared increases by 1. Determining good models "by inspection" may not sound reliable, but we could not avoid having to make some subjective decisions about which models could be considered acceptable, which has also been done in Magri et al. (2007); Magri et al. (2011); Nolan et al. (2013).

6.2 Shape Model

We present the first shape model of potentially hazardous asteroid 1981 Midas from lightcurve and radar observations. The final shape model of Midas is shown in Figure 6.3, and additional views of the model with comparisons to the data are shown in Appendix A. This model is made up of 532 vertices and has an average edge length of .19km. A collection of its properties is included in Table 6.1. For this final shape model, we ran a search around the pole position of the best fit model where we let axis lengths vary. To find the 1σ uncertainty for the primary axis dimensions, we ran a set of models with varying scale factors for each axis. By inspection, we found the uncertainty in each dimension to be where the reduced chi-squared increases by 1, which was 10%.

There are no preexisting shape models of Midas to compare to, but since Midas is a large, potentially hazardous asteroid, acquiring radar data should be prioritized in the next closest approach in 2032 (close approach of .086 au). Creating another model from these future observation will allow for a check on the accuracy of this model as well as the development of one with better radar coverage. Additionally, this model can be used for an orbital dynamics study to find stable orbits for potential natural satellites or spacecraft.

Table 6.1: Properties of 1981 Midas

Dimensions along principal axis (km)	X	$3.33 \pm 10\%$
	Y	$1.99 \pm 10\%$
	Z	$1.85 \pm 20\%$
Surface area (km^2)		$16.33 \pm 25\%$
Volume (km^3)		$4.26 \pm 35\%$
Diameter of volume equivalent sphere (km)		$2.01 \pm 12\%$
Pole ecliptic longitude (°)		$37° \pm 5°$
Pole ecliptic latitude (°)		$-61° \pm 6°$

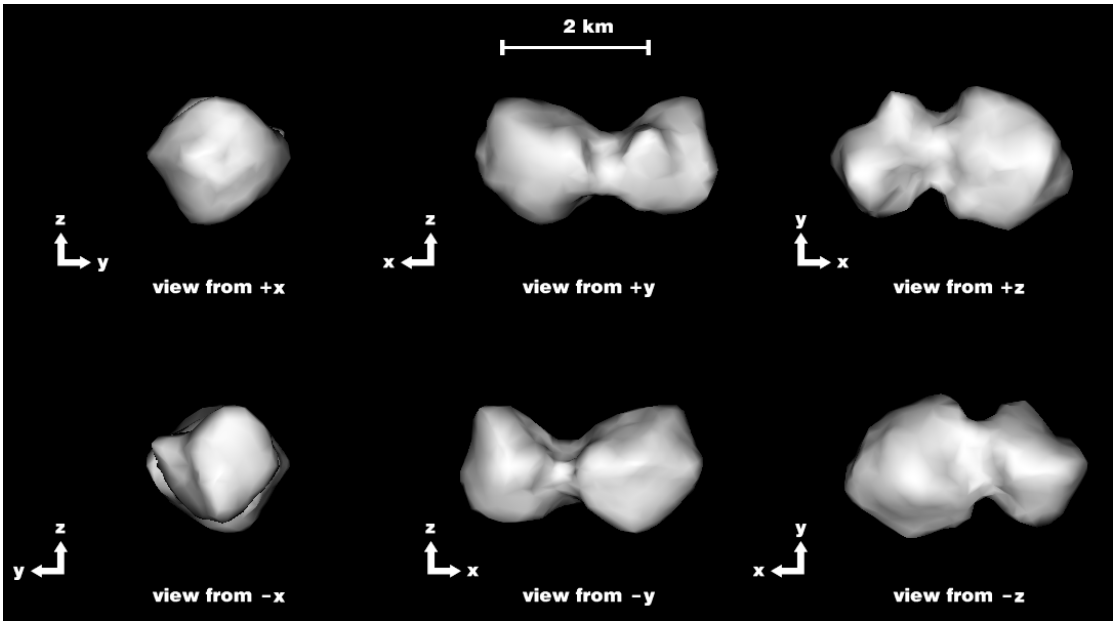

FIGURE 6.3: The final model of Midas as seen looking down each axis.

APPENDIX A: Selected Views of Model

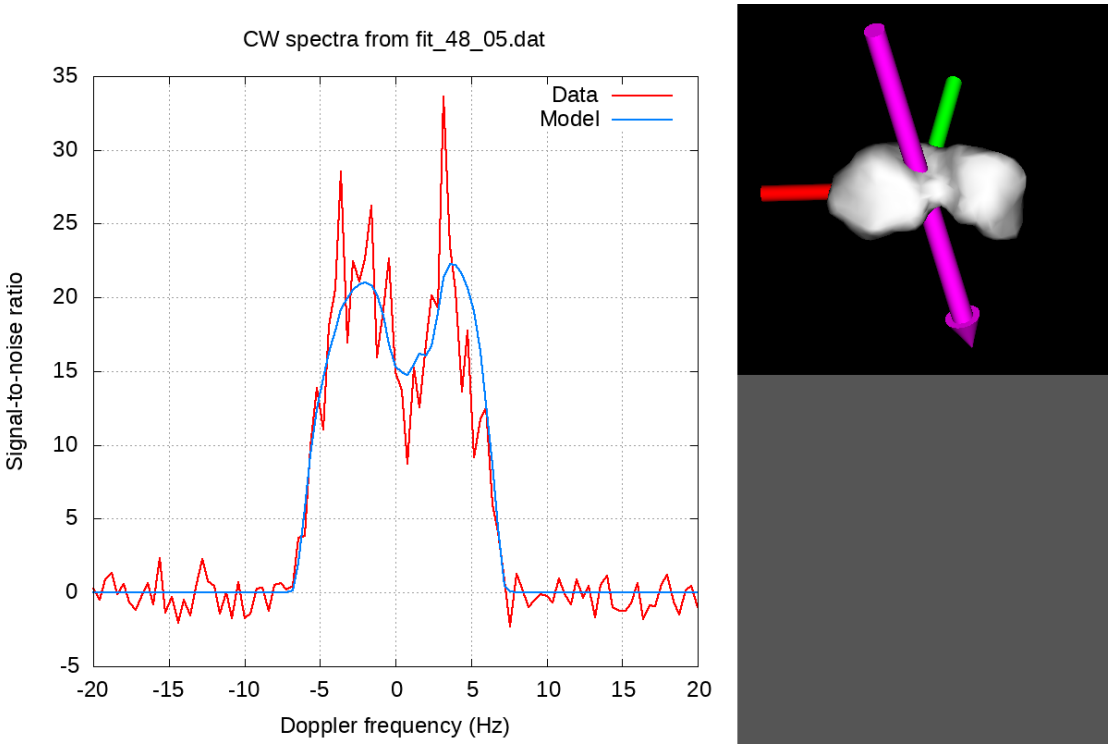

FIGURE A.1: Example CW spectra from March 25, 2018 in red with model spectra overlayed in blue and plane-of-sky view of Midas to the right. In the plane-of-sky view, the pink arrow shows the rotational axis and the red and green lines show the long and intermediate axes, respectively (the short axis is aligned with the rotational axis).

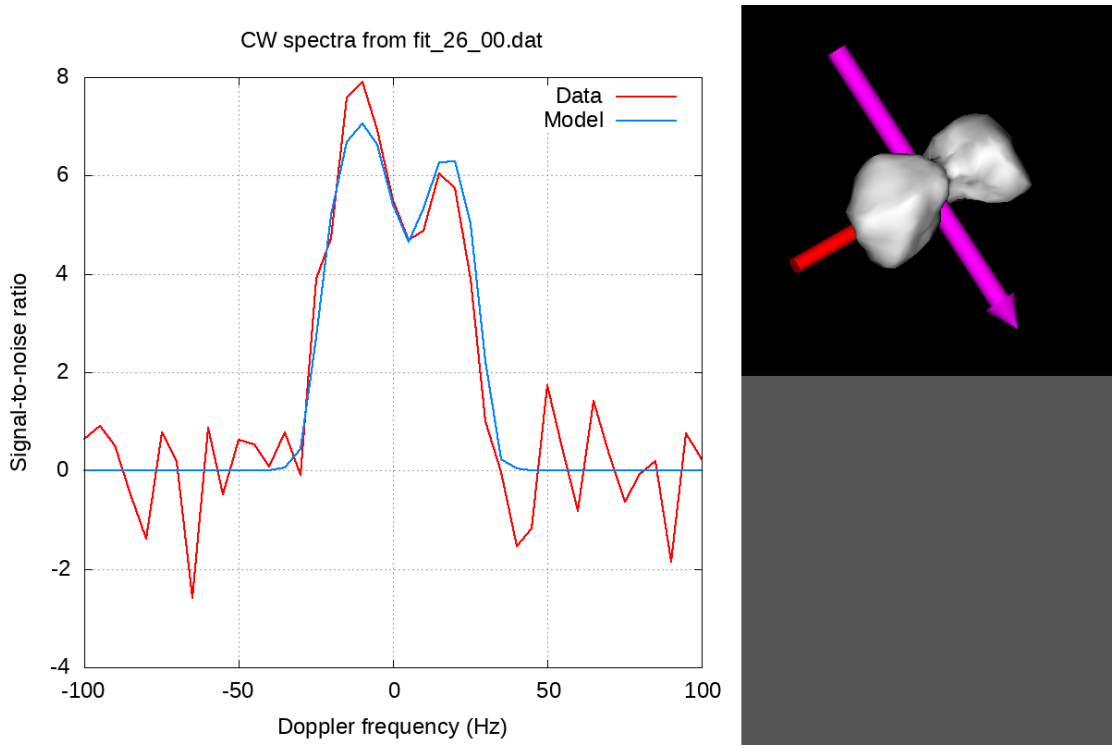

FIGURE A.2: Example CW spectra from March 21, 2018 in red with model spectra overlayed in blue and plane-of-sky view of Midas to the right. In the plane-of-sky view, the pink arrow shows the rotational axis and the red and green lines show the long and intermediate axes, respectively (the short axis is aligned with the rotational axis).

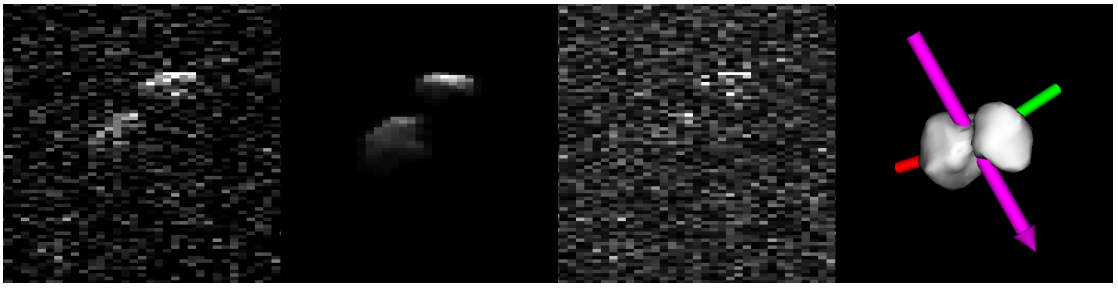

FIGURE A.3: From left to right: delay-Doppler image from March 21, 2018, corresponding delay-Doppler model image, residuals, plane-of-sky view of model. In the plane-of-sky view, the pink arrow shows the rotational axis and the red and green lines show the long and intermediate axes, respectively (the short axis is aligned with the rotational axis).

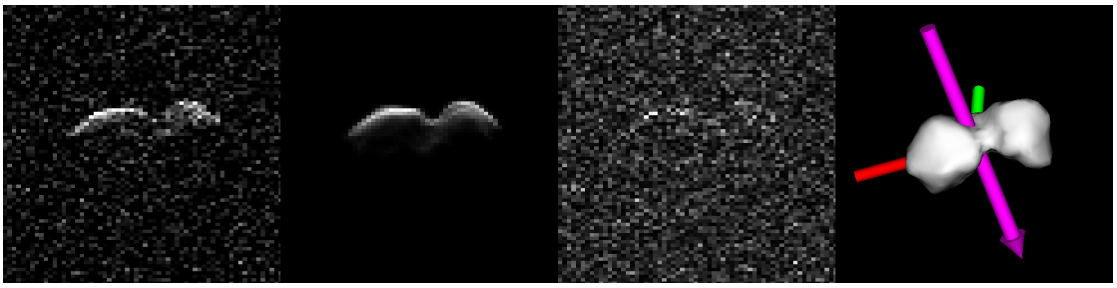

FIGURE A.4: From left to right: delay-Doppler image from March 23, 2018, corresponding delay-Doppler model image, residuals, plane-of-sky view of model. In the plane-of-sky view, the pink arrow shows the rotational axis and the red and green lines show the long and intermediate axes, respectively (the short axis is aligned with the rotational axis).

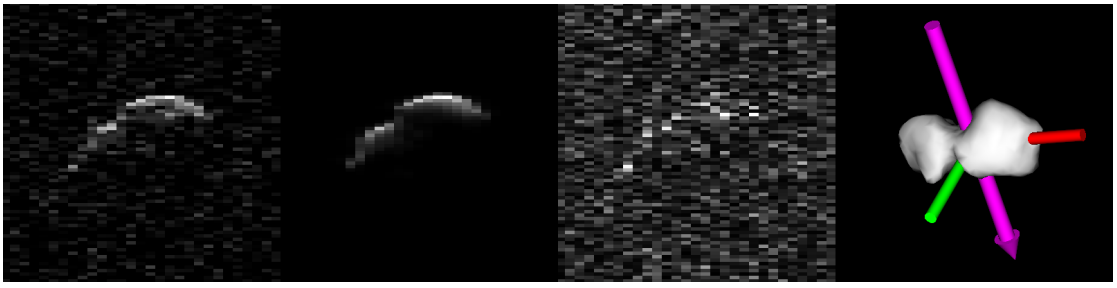

FIGURE A.5: From left to right: delay-Doppler image from March 24, 2018, corresponding delay-Doppler model image, residuals, plane-of-sky view of model. In the plane-of-sky view, the pink arrow shows the rotational axis and the red and green lines show the long and intermediate axes, respectively (the short axis is aligned with the rotational axis).

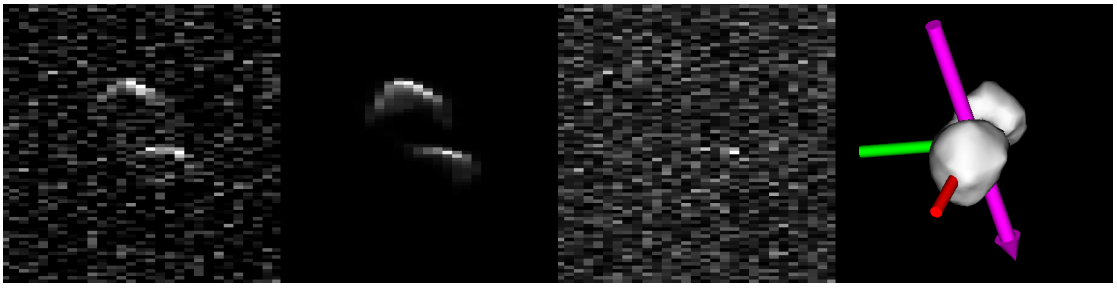

FIGURE A.6: From left to right: delay-Doppler image from March 24, 2018, corresponding delay-Doppler model image, residuals, plane-of-sky view of model. In the plane-of-sky view, the pink arrow shows the rotational axis and the red and green lines show the long and intermediate axes, respectively (the short axis is aligned with the rotational axis).

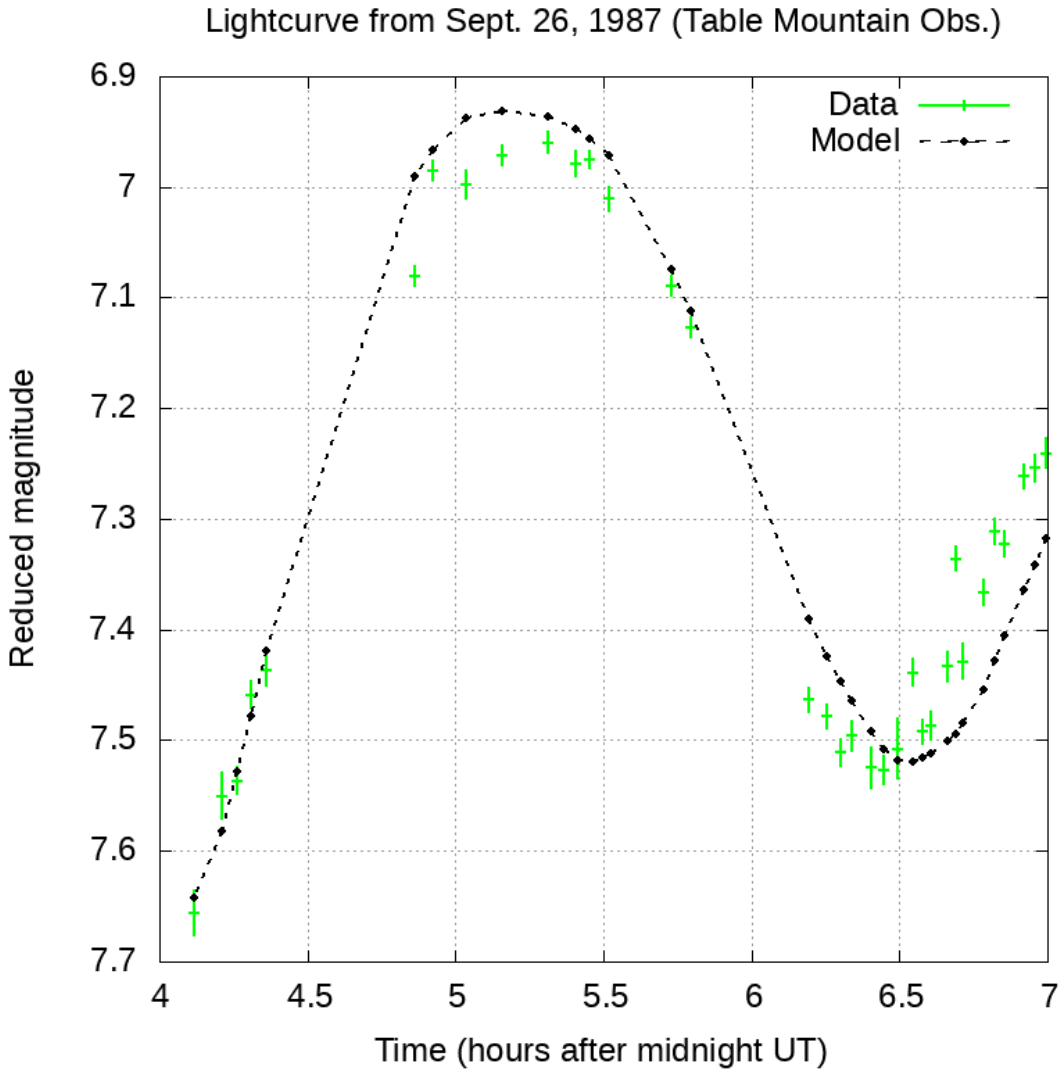

FIGURE A.7: Sample lightcurve from September 26, 1987 taken at Table Mountain Observatory in California. The data are plotted in green and the model's lightcurve is plotted in black points connected by a dotted line. In the plane-of-sky view, the pink arrow shows the rotational axis and the red and green lines show the long and intermediate axes, respectively (the short axis is aligned with the rotational axis).

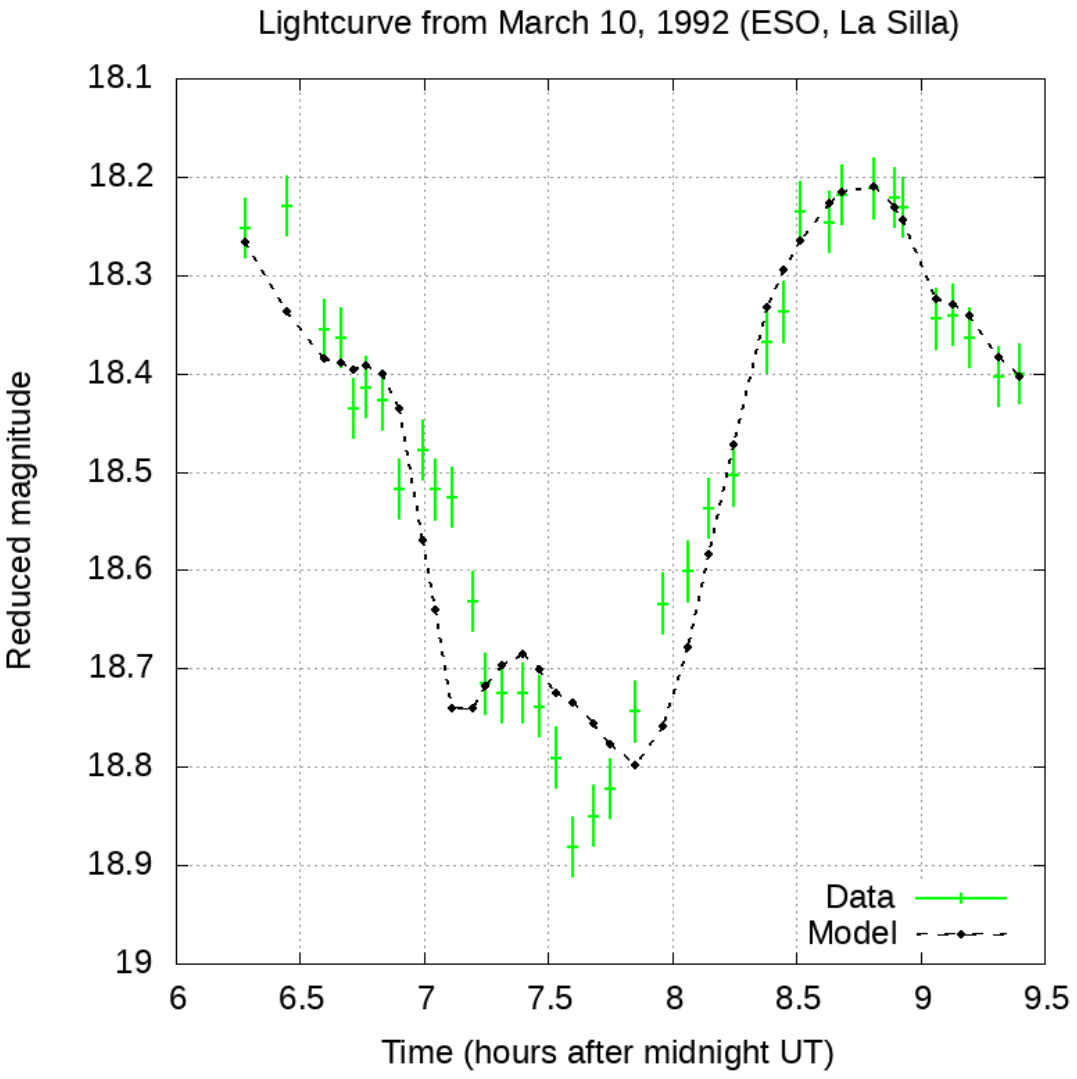

FIGURE A.8: Sample lightcurve from March 10, 1992 taken at the European Southern Observatory in Chile. The data are plotted in green and the model's lightcurve is plotted in black points connected by a dotted line.

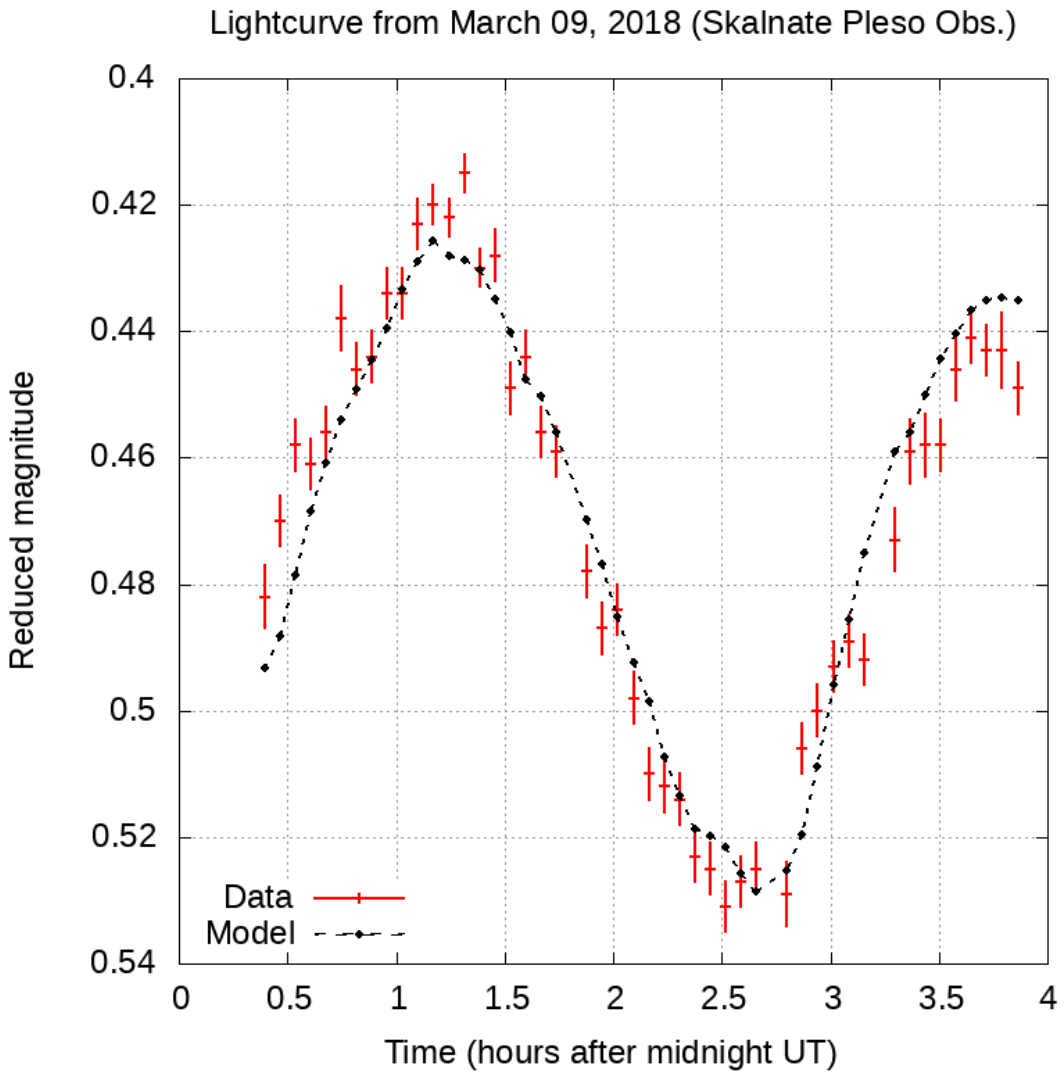

FIGURE A.9: Sample lightcurve from March 9, 2018 taken at the Skalnaté Pleso Observatory in Slovakia. The data are plotted in green and the model's lightcurve is plotted in black points connected by a dotted line.

Bibliography

Benner, L. A. M., Busch, M. W., Giorgini, J. D., Taylor, P. A., & Margot, J.-L. 2015, Radar Observations of Near-Earth and Main-Belt Asteroids, ed. P. Michel, F. E. DeMeo, & W. F. Bottke, 165–182

Binzel, R. P., Lupishko, D., di Martino, M., Whiteley, R. J., & Hahn, G. J. 2002, Physical Properties of Near-Earth Objects, ed. W. F. Bottke, Jr., A. Cellino, P. Paolicchi, & R. P. Binzel, 255–271

Binzel, R. P., Reddy, V., & Dunn, T. L. 2015, The Near-Earth Object Population: Connections to Comets, Main-Belt Asteroids, and Meteorites, ed. P. Michel, F. E. DeMeo, & W. F. Bottke, 243–256

Binzel, R. P., Rivkin, A. S., Stuart, J. S., et al. 2004, Icarus, 170, 259

Binzel, R. P., Morbidelli, A., Merouane, S., et al. 2010, in Lunar and Planetary Science Conference, Vol. 41, Lunar and Planetary Science Conference, 1226

Brozovic, M., Benner, L. A. M., Naidu, S. P., et al. 2016, in AAS/Division for Planetary Sciences Meeting Abstracts, Vol. 48, AAS/Division for Planetary Sciences Meeting Abstracts #48, 325.04

Bus, S. J., & Binzel, R. P. 2002a, Icarus, 158, 106

—. 2002b, Icarus, 158, 146

Carry, B., Solano, E., Eggl, S., & DeMeo, F. E. 2016, Icarus, 268, 340

Chapman, C. R., Morrison, D., & Zellner, B. 1975, Icarus, 25, 104

Crowell, J. L., Howell, E. S., Magri, C., et al. 2017, Icarus, 291, 254

DeMeo, F. E., Binzel, R. P., & Lockhart, M. 2014, Icarus, 227, 112

DeMeo, F. E., Binzel, R. P., Slivan, S. M., & Bus, S. J. 2009, Icarus, 202, 160

Fevig, R. A. 2006, PhD thesis, The University of Arizona

Franco, L., Marchini, A., Baj, G., et al. 2018, Minor Planet Bulletin, 45, 273

Giorgini, J. D., Benner, L. A. M., Brozovic, M., et al. 2009, Radar Astrometry of Small Bodies: Detection, Characterization, Trajectory Prediction, and Hazard Assessment, Tech. rep.

Greenstreet, S., Ngo, H., & Gladman, B. 2012, Icarus, 217, 355

Harcke, L. J. 2005, PhD thesis, Stanford University, California, USA

Harris, A. W., & D'Abramo, G. 2015, Icarus, 257, 302

Hudson, S. 1994, Remote Sensing Reviews, 8, 195

Lauretta, D. S., Balram-Knutson, S. S., Beshore, E., et al. 2017, Space Sci. Rev., 212, 925

Magri, C., Ostro, S. J., Scheeres, D. J., et al. 2007, Icarus, 186, 152

Magri, C., Howell, E. S., Nolan, M. C., et al. 2011, Icarus, 214, 210

Mainzer, A., Grav, T., Masiero, J., et al. 2012, ApJ, 752, 110

Mottola, S., Angelis, G. D., Martino, M. D., et al. 1995, Icarus, 117, 62

Muinonen, K., Torppa, J., Virtanen, J., et al. 2007, in IAU Symposium, Vol. 236, Near Earth Objects, our Celestial Neighbors: Opportunity and Risk, ed. G. B. Valsecchi, D. Vokrouhlický, & A. Milani, 309–320

Naidu, S. P., Benner, L. A. M., Margot, J.-L., Busch, M. W., & Taylor, P. A. 2016, AJ, 152, 99

Nakamura, T., Noguchi, T., Tsuchiyama, A., et al. 2011, AGU Fall Meeting Abstracts, P42A

National Research Council. 2010, Defending Planet Earth: Near-Earth-Object Surveys and Hazard Mitigation Strategies (Washington, DC: The National Academies Press), doi:10.17226/12842

Nesvorný, D., Jedicke, R., Whiteley, R. J., & Ivezić, Ž. 2005, Icarus, 173, 132

Nolan, M. C., Magri, C., Howell, E. S., et al. 2013, Icarus, 226, 629

Nolan, M. C., Al Asad, M. M., Barnouin, O. S., et al. 2019, in Asteroid Science in the Age of Hayabusa2 and OSIRIS-REx Conference, Asteroid Science in the Age of Hayabusa2 and OSIRIS-REx Conference, 2033

Ostro, S. J., Hudson, R. S., Benner, L. A. M., et al. 2002, Asteroid Radar Astronomy, ed. W. F. Bottke, Jr., A. Cellino, P. Paolicchi, & R. P. Binzel, 151–168

Perna, D., Dotto, E., Ieva, S., et al. 2016, AJ, 151, 11

Sanchez, J. A., Michelsen, R., Reddy, V., & Nathues, A. 2013, Icarus, 225, 131

Shepard, M. K., Benner, L. A. M., Ostro, S. J., et al. 2004, Icarus, 172, 170

Taylor, P. A., Rivera-Valentín, E. G., Benner, L. A. M., et al. 2019a, Planet. Space Sci., 167, 1

Taylor, P. A., Rivera-Valentin, E. G., Virkki, A. K., et al. 2019b, in Lunar and Planetary Science Conference, Vol. 50, Lunar and Planetary Science Conference, 2945

Tedesco, E. F., Williams, J. G., Matson, D. L., et al. 1989, AJ, 97, 580

Tholen, D. J. 1984, PhD thesis, University of Arizona, Tucson

Virkki, A., Muinonen, K., & Penttilä, A. 2014, Meteoritics and Planetary Science, 49, 86

Wisniewski, W., Michalowski, T., Harris, A., & McMillan, R. 1997, Icarus, 126, 395